

# Heavy-mass magnetic modes in pyrochlore iridates due to dominant Dzyaloshinskii-Moriya interaction

Ravi Yadav,<sup>1</sup> Manuel Pereiro,<sup>2</sup> Nikolay A. Bogdanov,<sup>1</sup> Satoshi Nishimoto,<sup>1</sup>  
Anders Bergman,<sup>2</sup> Olle Eriksson,<sup>2</sup> Jeroen van den Brink,<sup>1,3</sup> and Liviu Hozoi<sup>1</sup>

<sup>1</sup>*Institute for Theoretical Solid State Physics, IFW Dresden, Helmholtzstr. 20, 01069 Dresden, Germany*

<sup>2</sup>*Department of Physics and Astronomy, Uppsala University, Uppsala 751 20, Sweden*

<sup>3</sup>*Department of Physics, Technical University Dresden, 01062 Dresden, Germany*

(Dated: July 4, 2017)

Materials with strong spin-orbit interactions are presently a main target in the search for systems with novel magnetic properties. Magnetic anisotropies can be very large in such compounds, ranging from strongly frustrated Kitaev exchange in honeycomb iridates and the associated spin-liquid states to robust antisymmetric couplings in square-lattice  $\text{Sr}_2\text{IrO}_4$ . Here we predict from *ab initio* quantum chemistry calculations that another highly unusual regime is realized in pyrochlore iridium oxides: the nearest-neighbor Heisenberg interaction can vanish whilst the antisymmetric Dzyaloshinskii-Moriya exchange reaches values as large as 5 meV, a result which challenges common notions and existing phenomenological models of magnetic superexchange. The resulting spin excitation spectra reveal a very flat magnon dispersion in the Nd- and Tb-based pyrochlore iridates, suggesting the possibility of using these modes to store magnetic information. Indeed the magnetization dynamics indicates that these modes are unable to propagate out of the excitation region.

*Introduction.* The anisotropy of intersite spin interactions refers to the presence of different coupling strengths for different spin components  $S_i^\alpha$ ,  $S_j^\beta$  at sites  $i$  and  $j$  (where  $\alpha, \beta \in \{x, y, z\}$ ) but also to the coupling defined by the cross product  $\mathbf{S}_i \times \mathbf{S}_j$ . While the importance of anisotropic exchange has long been recognized in quantum magnetism, such terms were most often regarded as only small perturbations to the dominant, isotropic Heisenberg contribution. However, this view is now changing with the occurrence of both experimental and theoretical evidence for large or even prevailing anisotropic interactions in  $5d$  transition-metal compounds. In honeycomb  $\text{Na}_2\text{IrO}_3$ , for example, the intersite spin-coupling anisotropy shows up in the form of bond-dependent Kitaev interaction terms [1] — this symmetric anisotropic exchange defines in  $\text{Na}_2\text{IrO}_3$  the leading contribution to the effective spin Hamiltonian [2–4]. For nearest-neighbor (NN)  $\text{IrO}_6$  octahedra in  $\text{Sr}_2\text{IrO}_4$ , on the other hand, the key anisotropy is the antisymmetric coupling, also referred to as Dzyaloshinskii-Moriya (DM) component. It reaches impressively large values of  $\sim 15$  meV [2, 5–7], orders of magnitude larger than in, e.g., the isostructural ‘214’ cuprates [8–10].

The bending of the Ir-O-Ir links is sizable in  $\text{Sr}_2\text{IrO}_4$ , with bond angles of  $157^\circ$ . The departure from straight Ir-O-Ir bonds is, however, even more pronounced in the so called ‘227’ pyrochlore iridates  $R_2\text{Ir}_2\text{O}_7$ , where  $R$  stands for a trivalent rare-earth ion: Ir-O-Ir bond angles as low as  $119^\circ$  have been determined in this family of iridium oxide compounds [11]. For such a geometry, the isotropic exchange is presumably strongly reduced as compared to the case of straight bonds in  $\text{Ba}_2\text{IrO}_4$  [6, 12] or of moderate flexure as in  $\text{Sr}_2\text{IrO}_4$  [2, 5–7]. But the antisymmetric DM coupling is likely to pick up values comparable to those in  $\text{Sr}_2\text{IrO}_4$  — the very atypical situation may arise

where the DM interaction  $D$  even exceeds the Heisenberg  $J$ . The obvious question is then what kind of unconventional magnetic orders and excitations can emerge in this case. With  $D/J$  ratios of  $\sim 1$  and ferromagnetic (FM)  $J$ ’s, unusual skyrmionic excitations were recently predicted for the kagomé-like [111] planes of the pyrochlore lattice [13]. For particular regions in the parameter space those skyrmionic states are stable even at room temperature, which has potential for applications to logic devices or for data storage.

Few-layer [111] slab structures of 227 iridates are predicted to display in the magnetically ordered all-in/all-out (AIAO) configuration anomalous Hall effect [14], Chern insulator states [15], emergent domain-wall metallic states [16], and topological magnon bands [17]. Experimental indications of AIAO magnetic order have been recently reported for  $\text{Nd}_2\text{Ir}_2\text{O}_7$  [18–20],  $\text{Tb}_2\text{Ir}_2\text{O}_7$  [21],  $\text{Eu}_2\text{Ir}_2\text{O}_7$  [22], and  $\text{Sm}_2\text{Ir}_2\text{O}_7$  [23]. However, little is known with respect to the strength of the intersite magnetic couplings in 227 iridates. To access this kind of information, essential for a detailed understanding of the 227 iridate pyrochlores, we here employ many-body quantum chemistry *ab initio* methods. Subsequently we use classical Monte Carlo simulations to determine the magnetic ground state of the resulting effective spin Hamiltonian and perform calculations within linear spin-wave theory on noncollinear configurations to derive the magnon excitation spectra. We find that variation of the Ir-O-Ir bond angles, from  $>130^\circ$  in  $\text{Sm}_2\text{Ir}_2\text{O}_7$  and  $\text{Eu}_2\text{Ir}_2\text{O}_7$  [24] to  $119^\circ$  in  $\text{Nd}_2\text{Ir}_2\text{O}_7$  [11], induces dramatic modifications of the  $D/J$  ratio, from  $D/J < 0.2$  in  $\text{Sm}_2\text{Ir}_2\text{O}_7$  and  $\text{Eu}_2\text{Ir}_2\text{O}_7$  to  $D/|J| \gtrsim 3$  for bond angles around  $120^\circ$ . The latter result,  $D/J > 3$ , is outstanding and shows that, e.g., the topological magnon bands recently predicted for  $D/J > 0.7$  [17] can be indeed realized

in pyrochlore-derived bilayer nanostructures. These very large  $D/J$  values and the possibility of tuning the sign of the Heisenberg coupling by changing the bond angles single out the 227 iridates, either as bulk or thin films, as an ideal playground for the study of DM-driven quantum magnetism, a research area that holds promise both from the perspective of fundamental science [13–17] and at the level of device applications [13].

*Electronic-structure calculations.* The Ir ions form a network of corner-sharing regular tetrahedra in the pyrochlore iridates, as sketched in Fig. 1. The lattice constant ( $a$ ) of the *fcc* unit cell varies in the range of 1–1.05 nm in these compounds. In addition to the  $a$  parameter, one other important structural detail is the fractional coordinate  $x$  of the O anion at the  $48f$  site [24], which determines the amount of trigonal distortion of the  $O_6$  octahedral cage around each Ir cation: cubic, undistorted O octahedra are realized only for  $x = x_c = 5/16$ . The  $x$  parameter is always larger than  $x_c$  in the 227 iridates, which translates into trigonal squashing of the ligand cages and Ir-O-Ir bond angles  $\theta < \theta_c = 141.1^\circ$ . The strong bending of Ir-O-Ir links and the angle  $\theta$  are highlighted in Fig. 1.

The Ir  $5d$ -shell formal oxidation state is  $4+$ , with one hole in the  $t_{2g}$  sublevels. In the presence of strong spin-orbit coupling (SOC), the latter are split into fully occupied  $j_{\text{eff}} \approx 3/2$  and half-filled  $j_{\text{eff}} \approx 1/2$  spin-orbit states [2]. To determine the strength of the various exchange interactions between such NN  $1/2$ -pseudospins, we carried out many-body quantum chemistry calculations for fragments of two corner-sharing  $\text{IrO}_6$  octahedra. We used energy-consistent relativistic core-level pseudopotentials plus valence basis functions of quadruple-zeta quality for Ir, all-electron quintuple-zeta basis sets for the bridging O ligand, and triple-zeta basis sets for the other ten O ions of the two-octahedra block (see Appendix for further details). Multiconfigurational wave functions were

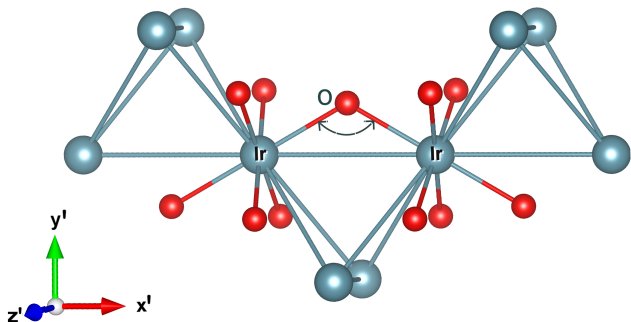


FIG. 1. Ir- and O-ion distribution within the  $R_2\text{Ir}_2\text{O}_7$  pyrochlore lattice. The network of corner-sharing  $\text{Ir}_4$  tetrahedra (larger blue spheres) and the O ligands around two NN Ir sites (smaller red spheres) are emphasized. Two adjacent  $\text{IrO}_6$  octahedra share a single O ion. The choice of the local coordinate system  $\{x', y', z'\}$  is discussed in the text.

TABLE I. Intersite effective spin couplings (meV) as derived from spin-orbit MRCI calculations in various 227 iridates. The form of the effective spin Hamiltonian and the choice of the coordinate system are described in the text.

	$\angle(\text{Ir-O-Ir})$	$J$	$D$	$\Gamma_{x'x'}$	$\Gamma_{y'y'}$
$\text{Sm}_2\text{Ir}_2\text{O}_7$	132	22.4	2.2	-1.7	-0.58
$\text{Eu}_2\text{Ir}_2\text{O}_7$	131	19.3	2.4	-2.0	-0.49
$\text{Y}_2\text{Ir}_2\text{O}_7$	130	18.8	2.6	-2.2	-0.46
$\text{Er}_2\text{Ir}_2\text{O}_7$	129	13.5	3.1	-2.4	-0.35
$\text{Lu}_2\text{Ir}_2\text{O}_7$	126	8.9	3.6	-2.9	0.31
$\text{Tb}_2\text{Ir}_2\text{O}_7$	121	-1.5	4.7	-3.4	-0.06
$\text{Nd}_2\text{Ir}_2\text{O}_7$	119	-1.6	5.1	-3.8	0.02

first obtained by complete-active-space self-consistent-field (CASSCF) calculations [25] for this  $[\text{Ir}_2\text{O}_{11}]$  fragment. The variational optimization was performed for an average of the lowest nine singlet and nine triplet states, mostly of  $t_{2g}^5-t_{2g}^5$  character. However, since intersite excitations of  $t_{2g}^4-t_{2g}^6$  type contribute with finite weight to the CASSCF wave functions, the CASSCF calculations account not only for NN  $t_{2g}^5-t_{2g}^5$  direct exchange but also for  $t_{2g}^4-t_{2g}^6$  superexchange processes. Further, additional superexchange paths involving the Ir  $5d$   $e_g$  or/and the oxygen  $2p$  orbitals show up in the subsequent multireference configuration-interaction (MRCI) computations [25]. The latter include all possible single and double electron excitations out of the Ir  $5d$   $t_{2g}$  and bridging-ligand  $2p$  shells.

All nine  $t_{2g}^5-t_{2g}^5$  triplet and low-lying nine singlet states enter the spin-orbit treatment, both at the CASSCF and MRCI level. The mapping of the *ab initio* quantum chemistry data onto the effective spin model implies however only the lowest four spin-orbit states, associated with the different possible couplings of two  $1/2$  pseudospins. The other 32 spin-orbit states in this manifold involve  $j_{\text{eff}} \approx 3/2$  to  $j_{\text{eff}} \approx 1/2$  charge excitation and lie at  $\gtrsim 0.5$  eV higher energy [2, 26].

*Magnetic model Hamiltonian.* A pair  $\langle ij \rangle$  of NN  $j_{\text{eff}} \approx 1/2$  sites is magnetically described by the following bilinear effective spin Hamiltonian:

$$\mathcal{H}_{\text{eff}}^{i,j} = J \tilde{\mathbf{S}}_i \cdot \tilde{\mathbf{S}}_j + \mathbf{D} \cdot \tilde{\mathbf{S}}_i \times \tilde{\mathbf{S}}_j + \tilde{\mathbf{S}}_i \cdot \bar{\Gamma} \cdot \tilde{\mathbf{S}}_j + \mu_B \sum_{k=i,j} \mathbf{h} \cdot \bar{\mathbf{g}}_k \cdot \tilde{\mathbf{S}}_k, \quad (1)$$

where  $\tilde{\mathbf{S}}_i$ ,  $\tilde{\mathbf{S}}_j$  are pseudospin- $1/2$  operators,  $J$  is the isotropic Heisenberg coupling,  $\mathbf{D}$  stands for the antisymmetric DM exchange,  $\bar{\Gamma}$  is a symmetric traceless second-rank tensor defining the symmetric anisotropic interaction, and the last term describes the coupling to an external magnetic field  $\mathbf{h}$ . The anisotropy of the latter component is characterized by the  $\bar{\mathbf{g}}$  tensor.

Since a block of two NN  $\text{IrO}_6$  octahedra has  $C_{2v}$  point-group symmetry in 227 pyrochlore iridates, with two-fold rotational symmetry around the Ir-Ir axis (see Fig. 1), a

convenient reference system is for many purposes a local frame having one of the coordinates along the line defined by those two Ir sites. Such a coordinate system,  $\{x', y', z'\}$ , is used in Fig. 1 and form part of the following discussion, with the  $x'$  axis taken along the Ir-Ir link and  $z'$  perpendicular to the triangular plaquette formed by the two Ir NN's and the bridging ligand. In this frame, all off-diagonal elements  $\Gamma_{\alpha\beta}$  are 0 and we can then write [4, 7]

$$\bar{\Gamma} = \begin{pmatrix} \Gamma_{x'x'} & 0 & 0 \\ 0 & \Gamma_{y'y'} & 0 \\ 0 & 0 & -\Gamma_{x'x'} - \Gamma_{y'y'} \end{pmatrix}. \quad (2)$$

The  $C_{2v}$  symmetry further simplifies the form of the DM vector, with  $\mathbf{D} = (0, 0, D)$ . It is the effective spin model described by Eqs. (1) and (2) onto which we map the *ab initio* quantum chemistry data for the spin-orbit, two-octahedra  $d^5-d^5$  states (see [7, 27] and Appendix for details). Intersite magnetic couplings based on spin-orbit MRCI calculations and such a mapping scheme are provided in Table I.

In contrast to usual plots in which various quantities are pictured as function of the  $R$ -ion radius [28], we focus in Table I on overall trends when gradually reducing the Ir-O-Ir bond angle. In addition to the lanthanide-based 227 iridates, we also include in the table the Y-iridate,  $Y_2Ir_2O_7$ .

From the MRCI results listed in Table I it is seen that the  $\Gamma$  coupling parameters are never the largest inter-

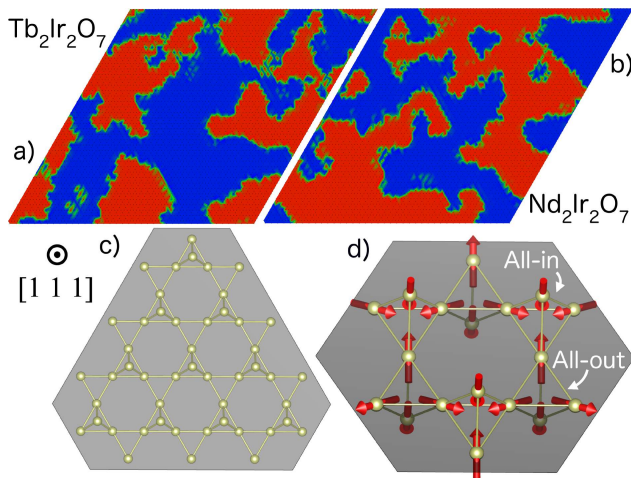


FIG. 2. Ground-state spin structures in 227 iridates. Computational results for Tb227 and Nd227 are provided in (a) and (b), respectively, for planar atomic configurations of  $40 \times 40$  unit cells normal to the  $[111]$  crystallographic direction. The blue and red sectors represent different orientations of the  $z$  components of the Ir magnetic moments, parallel or antiparallel to the  $z$  axis. The transition region between those sectors is highlighted in green. A kagomé Ir plane onto which the magnetic moments in (a) and (b) are mapped is sketched in (c) while (d) displays the AIOA spin arrangement found for the other iridates studied here.

TABLE II. Intersite effective spin couplings (meV) at different levels of theory for the smallest ( $Nd_2Ir_2O_7$ ) and largest ( $Sm_2Ir_2O_7$ ) Ir-O-Ir bond angles reported in 227 iridates [11, 24].

227 system	Method	$J$	$D$	$\Gamma_{x'x'}$	$\Gamma_{y'y'}$
$Sm_2Ir_2O_7$	MRCI	22.4	2.2	-1.7	-0.6
	CASSCF	11.5	1.2	-0.9	0.2
	ROHF	-1.2	0.3	-0.2	1.2
$Nd_2Ir_2O_7$	MRCI	-1.6	5.1	-3.8	0.02
	CASSCF	-1.8	4.6	-2.3	-0.3
	ROHF	-0.4	0.4	-0.2	0.2

actions. The overall tendencies for the other exchange couplings are obvious: from  $J$  and  $D$  values in the range  $J > 20$  and  $D > 2$  meV for the largest Ir-O-Ir bond angles, one arrives at  $J \approx -1.5$  and  $D \approx 5$  meV for bond angles of  $119-121^\circ$  in  $Nd_2Ir_2O_7$  and  $Tb_2Ir_2O_7$ . In other words, the  $D/J$  ratio changes by a factor of  $\approx 30$  along the series, with the highly unusual situation of having a DM interaction  $D$  a few times larger than the Heisenberg  $J$  in  $Nd_2Ir_2O_7$  and  $Tb_2Ir_2O_7$ . What is more interesting,  $J$  changes sign for Ir-O-Ir angles of  $121-125^\circ$ . This suggests that even larger  $D/J$  ratios are in principle attainable by using strain in thin films of 227 iridates or pressure, to reach angles in the  $121-125^\circ$  interval for which  $J \rightarrow 0$ .

*Emergent domain-wall state.* Starting from the effective coupling parameters displayed in Table I, the magnetic ground-state configurations of the series of 227 iridates were computed in a two-stage approach. In a first step, classical Monte Carlo simulated annealing [29] was used to ‘thermalise’ the system, at a temperature of 0.001 K. Data sampling was subsequently performed by using an atomistic spin dynamics (ASD) method, as implemented in the UppASD code (see [30] and Appendix for further information). With the exception of Tb227 and Nd227, the atomic spin moments of the resulting ground-state magnetic structures follow a AIOA pattern, see Fig. 2.(d). Plots for the orientation of the  $z$  components of the magnetic moments, “+ $z$ ” and “- $z$ ”, at sites within a plane perpendicular to the  $[111]$  crystallographic direction [24] are provided in Figs. 2.(a)-(b) for both  $Tb_2Ir_2O_7$  and  $Nd_2Ir_2O_7$ . The spin configuration is collinear and FM in each of the blue (+ $z$ ) and red (- $z$ ) sectors and there is a transition region (shown in green color) where the moments rotate continuously from parallel orientation in blue to antiparallel in red, giving rise to an *emergent domain-wall state* [16]. The arrangement of Ir sites within a kagomé plane of the pyrochlore lattice is depicted in Fig. 2.(c). Such a plane has been chosen for the plots in Figs. 2.(a)-(b). The degenerate magnetic ground state associated with the domain-wall structure can be destroyed by small magnetic fields applied along the  $[111]$  crystallographic direction.

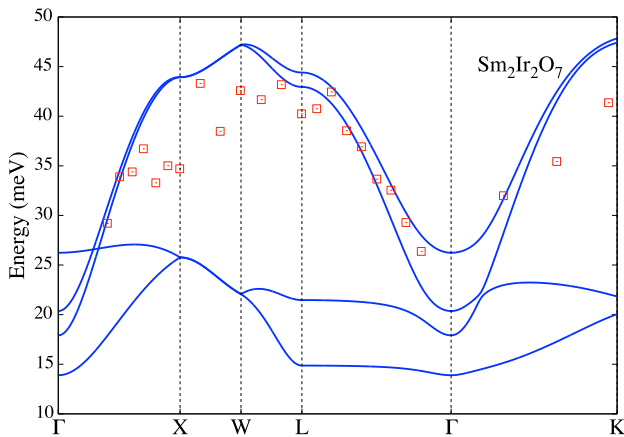


FIG. 3. Adiabatic magnon spectrum of  $\text{Sm}_2\text{Ir}_2\text{O}_7$  (blue lines). The empty squares indicate the experimental data of Ref. [23]. The four different branches are related to the four inequivalent Ir sites in the unit cell.

We note that the  $R$ -ion magnetic sublattice, believed to actively contribute to the realization of AIAO order in  $R_2\text{Ir}_2\text{O}_7$  pyrochlores [18–21], is not accounted for in our computations. In other words, for a given  $D/J$  ratio, our simulations would somewhat overestimate the tendency towards the formation of domain-wall states. But this instability is there, ‘nearby’ and further modification of the  $D/J$  ratio through appropriate engineering of the Ir-O-Ir angle, via either strain or pressure, should drive some of these materials towards that kind of regime. According to our MRCI results, the most ‘responsive’ should be the Tb227, Nd227, and Lu227 systems.

*Spin dynamics.* It is instructive to confront these theoretical results and predictions with measurements on the properties of the magnetic system in pyrochlore iridates. In particular, spin excitation spectra have been recently measured for  $\text{Sm}_2\text{Ir}_2\text{O}_7$  [23] using resonant inelastic x-ray scattering (RIXS). For comparison, we show in Fig. 3 the adiabatic magnon spectra of  $\text{Sm}_2\text{Ir}_2\text{O}_7$  as calculated for a noncollinear magnetic ground state, using linear spin wave theory (LSWT) and the UppASD computer implementation. The spectra were obtained on the basis of the effective coupling parameters of Table I and a moment  $0.75 \mu_B$  at each Ir site. It is seen that the theoretical magnon spectrum agrees well with the experimental data reported in Ref. [23]. The gap of the acoustical branch is due to having both large DM and symmetric anisotropic couplings. Donnerer *et al.* [23] found that a rather good fit of the experimental dispersion is obtained by LSWT and  $J=27$ ,  $D=4.9$  meV. Our *ab initio* results for  $\text{Sm}_2\text{Ir}_2\text{O}_7$ ,  $J \approx 22.5$  and  $D=2.2$  meV (see Table I), are somewhat on the lower side, as compared to the outcome of the LSWT fits in Ref. [23]. However, analysis of the quantum chemistry data at different levels of approximation — restricted open-shell Hartree-Fock (ROHF) [25], CASSCF, and MRCI (see Table II)

— shows that while the corrections brought by MRCI to CASSCF are important for large Ir-O-Ir angles, they are minor for the lowest bond angles, in the range of only tenths of a meV. This implies that our prediction of small, FM  $J$  values for strongly bent Ir-O-Ir links in  $\text{Nd}_2\text{Ir}_2\text{O}_7$  and  $\text{Tb}_2\text{Ir}_2\text{O}_7$  is solid. MRCI results in good agreement with experimental data were earlier reported using the same quantum chemistry approach for corner-sharing  $\text{IrO}_6$  octahedra with Ir-O-Ir bond angles of  $180^\circ$  in  $\text{Ba}_2\text{IrO}_4$  [12],  $157^\circ$  in  $\text{Sr}_2\text{IrO}_4$  [7], and  $140^\circ$  in  $\text{CaIrO}_3$  [31]. Remarkably large variations of the anisotropic interactions as function of bond angles were also computed for edge-sharing octahedra in honeycomb iridates [32], with the Kitaev coupling evolving between  $\approx 0$  meV at  $90^\circ$ , an *ab initio* result which challenges present superexchange models [2], to  $\approx 25$  meV for  $100^\circ$ .

Adiabatic magnon spectra computed for other pyrochlore iridates of the 227 family are provided in Fig. 4.(a)-(b) and in Supplementary Information. The spectra of Sm227, Eu227, Er227, Lu227, and Y227 display very similar features, see Figs. 3 and S1, as all these compounds possess the same type of AIAO magnetic order. Nd227 and Tb227, on the other hand, exhibit an instability towards the formation of emergent domain-wall states. Magnon spectra for the case of collinear FM ground states are displayed for these two materials in Fig. 4. Interestingly, both spectra feature very flat (nearly degenerate) bands at intermediate energies along the  $L \rightarrow \Gamma$  direction [red ellipses in Figs. 4.(a)-(b)]. A nearly vanishing magnon dispersion in the  $L \rightarrow \Gamma$  sector brings the prospect of using magnetic excitations which reverse the orientation of the magnetic moments for storing permanent magnetic information. Along this line of thinking, we show in Fig. 4.(d) the Ir-site magnetic moments averaged over a simulation time of 82 ps. The region in red color indicates an area where the Ir moments are constant in time, pointing out of the kagomé [111] plane, while blue color illustrates a strong magnetic perturbation that reverses the magnetization direction. The evolution in time of the spin system was modeled according to the Landau-Lifshitz-Gilbert (LLG) equation of motion, after the system was thermalised at a very low temperature ( $10^{-3}$  K). A time-dependent external magnetic field with a frequency corresponding to the energy range in which the Nd227 magnon spectra are flat (32.34 meV) was applied in the simulation, within a limited domain of  $6 \times 6 \times 1$  unit cells. Moreover, the external field was applied along the [1 1 1] direction, which corresponds to the direction  $L \rightarrow \Gamma$  in reciprocal space. As shown in Fig. 4.(d), the magnetic perturbation is not able to propagate out of the excitation region. In other words, any perturbation that reverses the orientation of the moments will stay localised in this area, without propagation or dissipation via spin-waves.

*Conclusions.* The microscopic mechanism through which spin-orbit interactions give rise to anisotropic ex-

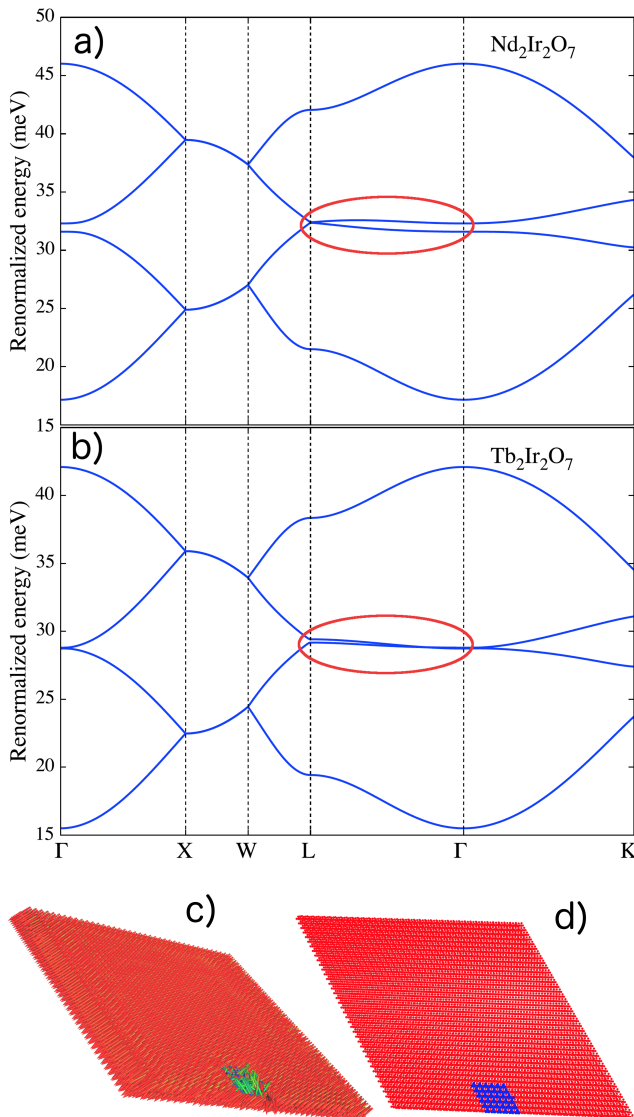


FIG. 4. Adiabatic magnon spectra for (a) Nd277 and (b) Tb277. The region with almost flat bands is indicated with a red ellipse. (c) Snapshot after applying a time-dependent external magnetic field in Nd277. The external perturbation is applied locally, within a region of approximately  $6 \times 6 \times 1$  unit cells; the sampled volume is  $40 \times 40 \times 3$  unit cells. ‘Perturbed’ spins are indicated in green color. (d) Time-averaged magnetic moments. Magnon activity is indicated in blue color.

change in magnetic insulators represents a longstanding problem. With regard to the antisymmetric anisotropy, also referred to as the Dzyaloshinskii-Moriya term, a large body of theoretical studies focused so far on extensions of the Hubbard model and layered square-lattice materials such as  $\text{La}_2\text{CuO}_4$  [8–10] and  $\text{Sr}_2\text{IrO}_4$  [2, 5, 6]. As a rule of thumb,  $D \ll J$ , with  $D$  values three orders of magnitude smaller than  $J$  in cuprates [10]. More recently, Dzyaloshinskii-Moriya interaction strengths of 20–25% of the Heisenberg  $J$  have been estimated in  $\text{Sr}_2\text{IrO}_4$  [2, 5–7]. Here we employ *ab initio* quantum-chemistry many-body

techniques to reveal a singular situation in which the Dzyaloshinskii-Moriya coupling parameter  $D$  outstrips the isotropic Heisenberg interaction. This is achieved according to our calculations in the pyrochlore iridates  $\text{Nd}_2\text{Ir}_2\text{O}_7$  and  $\text{Tb}_2\text{Ir}_2\text{O}_7$ , displaying strongly bent Ir-O-Ir links with bond angles of less than  $125^\circ$ . We further show that such a regime is prone to the formation of emergent domain-wall states. In our computations both  $\text{Nd}_2\text{Ir}_2\text{O}_7$  and  $\text{Tb}_2\text{Ir}_2\text{O}_7$  feature magnon dispersions that are almost zero along specific directions. This points to the potential use of magnetic excitations which reverse the orientation of the magnetic moments to store magnetic information. Indeed, the calculated magnetization dynamics shows that these excited magnetic modes are unable to propagate out of the excitation region.

*Acknowledgements.* Calculations were performed at the High Performance Computing Center (ZIH) of the Technical University Dresden (TUD) and at the computational facilities of C3SE at Chalmers University of Technology in Gothenburg, under a project administrated by SNIC/SNAC. R. Y., S. N., and L. H. thank U. Nitzsche for technical assistance. L. H. thanks P. Fulde and U. Röbller for discussions. We acknowledge financial support from the German Science Foundation (Deutsche Forschungsgemeinschaft, DFG — SFB-1143 and HO-4427/2), the KAW Foundation (projects 2013.0020, 2012.0031), the Swedish Research Council (VR), and eSENCE.

## Appendix

*Ab initio calculations.* As concerns the quantum chemistry calculations, the material model consists of two  $\text{IrO}_6$  octahedra sharing one ligand, with bond lengths and bond angles as determined experimentally [11, 21, 24]. A similar material model has been used in earlier work to establish the strengths of the Kitaev and Heisenberg effective couplings and their dependence on bond angles for edge-sharing octahedra in honeycomb-lattice iridates [4]. We applied energy-consistent relativistic pseudopotentials along with basis sets of quadruple-zeta quality [33] for the two Ir sites of the reference octahedra. All-electron basis sets of quintuple-zeta quality were used for the bridging oxygen, while triple-zeta basis functions were used for the remaining oxygen atoms of the reference octahedra [34]. We further employed two Ir  $f$  [33] and four O  $d$  [34] polarization functions for the two central Ir ions and the bridging  $\text{O}_b$  ligand, respectively.

In the initial step, multiconfiguration wave functions were generated by CASSCF calculations where 10 electrons (5 at each  $\text{Ir}^{4+}$  site) and 6  $t_{2g}$  orbitals (3 at each  $\text{Ir}^{4+}$  site) were considered in the active space. The CASSCF optimization was carried out for the low-lying nine sin-

glets and the nine triplets belonging to this manifold. All these states entered the subsequent spin-orbit calculations [35], both at the CASSCF and MRCI level. In the MRCI treatment, we accounted for single and double excitations from the Ir  $t_{2g}$  and bridging O<sub>b</sub>  $2p$  orbitals [36, 37]. A Pipek-Mezey localization procedure [38] was employed for separating the metal  $5d$  and O  $2p$  valence orbitals into different groups (e.g., bridging and non-bridging  $p$  orbitals). All calculations were performed with the MOLPRO quantum chemistry package [39]. A similar computational strategy has been successfully adopted in earlier quantum chemistry studies [4, 7, 27].

*Mapping procedure.* The lowest four spin-orbit states obtained from the *ab initio* quantum chemistry calculations are mapped onto the respective eigenvectors of the effective spin model defined by Eq. (1). To illustrate the way the mapping procedure is carried out, relevant matrix elements are provided in Tables III and IV for Sm<sub>2</sub>Ir<sub>2</sub>O<sub>7</sub>. Each of the matrix elements  $H_{ab\textit{ initio}}^{kl}$  computed at the quantum chemistry level, see Table III, is assimilated to the corresponding matrix element  $H_{\textit{eff}}^{kl}$  of the effective spin Hamiltonian, see Table IV. This one-to-one correspondence between *ab initio* and effective-model matrix elements enables the evaluation of all coupling constants in Eq. (1).

For  $C_{2v}$  symmetry of the two-octahedra [Ir<sub>2</sub>O<sub>11</sub>] unit, it is convenient to choose a reference frame with one of the axes along the Ir-Ir link. The data shown in Tables III and IV are expressed by using such a coordinate system, with the  $x'$  axis along the Ir-Ir segment and  $z'$  perpendicular to the Ir-O<sub>b</sub>-Ir plane. In this framework, the  $\bar{\mathbf{g}}$  tensor describing the Zeeman interaction term in Eq. (1) takes the following form at each Ir site  $k \in \{i, j\}$  [40, 41]:

$$\bar{\mathbf{g}}_k = \begin{pmatrix} g_{x'x'} & g_{x'y'} & 0 \\ g_{x'y'} & g_{y'y'} & 0 \\ 0 & 0 & g_{z'z'} \end{pmatrix}. \quad (3)$$

Since the Zeeman coupling to an external magnetic field can be also expressed as  $\hat{\mathcal{H}}_Z^{i,j} = \mu_B(\mathbf{L} + g_e\mathbf{S}) \cdot \mathbf{h}$ , all required matrix elements can be easily obtained on the basis of the MOLPRO output data, i.e., the expectation values of the total angular-momentum ( $\mathbf{L}$ ) and spin ( $\mathbf{S}$ ) operators (see also Refs. [7, 27]).  $\Delta_+$  and  $\Delta_-$  stand in Table IV for

$$\Delta_{\pm} = 2J + \Gamma_{x'x'} \pm \sqrt{4D^2 + (2J + \Gamma_{x'x'})^2}. \quad (4)$$

*Spin dynamics and LSWT for noncollinear systems.* In order to calculate the ground-state magnetic configurations of the series of 227 iridates, we used in the initial stage classical Monte Carlo simulated annealing [29] to thermalise the system. Subsequently, data sampling was performed by ASD simulations [30]. During the annealing process the initial temperature was fixed to 500 K and then reduced in the sequence 500–300–100–50 K to the

very last step where the targeted temperature was 0.001 K. In order to thermalise the system, we used 100,000 Monte Carlo steps for each temperature.

The equation of motion of the classical atomistic spins reads in the LLG frame:

$$\begin{aligned} \frac{\partial \mathbf{s}_i}{\partial t} = & -\frac{\gamma}{1 + \alpha_i^2} \mathbf{s}_i \times [\mathbf{B}_i + \mathbf{b}_i(t)] \\ & - \frac{\gamma \alpha_i}{s(1 + \alpha_i^2)} \mathbf{s}_i \times \{\mathbf{s}_i \times [\mathbf{B}_i + \mathbf{b}_i(t)]\}, \end{aligned} \quad (5)$$

where  $\gamma$  is the gyromagnetic ratio,  $\alpha_i$  denotes a dimensionless site-resolved damping parameter which accounts for the energy dissipation that eventually brings the system into thermal equilibrium, the effective field is calculated as  $\mathbf{B}_i = -\partial \mathcal{H}_{\textit{eff}} / \partial \mathbf{s}_i$ , and temperature ( $T$ ) fluctuations are considered through a random Gaussian-shaped field  $\mathbf{b}_i(t)$ . To calculate the ground-state magnetic configurations we assumed a Gilbert damping  $\alpha=0.1$ , which allows to reach the ground-state in a short period of time. The total simulation time was 320 ps.

The adiabatic magnon spectra were derived within the LSWT frame for a noncollinear ground-state magnetic structure, following a strategy similar to that described in Ref. [42]. For the case of AIAO order the crystallographic unit cell is commensurate with the magnetic cell and consequently we defined a local coordinate system that transforms the AIAO configuration into FM order, by applying a rotation  $\mathcal{R}$  on every moment within the crystallographic unit cell. This rotation is applied to the spin Hamiltonian described by Eq. (1) and provides:

$$\begin{aligned} \mathcal{H} = \sum_{ij} & \left( \sqrt{\frac{s_i}{2}} (\mathbf{u}_i^T a_i + \mathbf{u}_i^T a_i^\dagger + \mathbf{v}_i^T (s_i - a_i^\dagger a_i)) \right) \mathcal{J}_{ij} \\ & \left( \sqrt{\frac{s_j}{2}} (\mathbf{u}_j^T a_j + \mathbf{u}_j^T a_j^\dagger + \mathbf{v}_j^T (s_j - a_j^\dagger a_j)) \right), \end{aligned} \quad (6)$$

where  $a_i^\dagger/a_i$  are bosonic operators that decrease/increase the spin quantum number and  $s_i$  is the modulus of the classical spin vector at atomic position  $i$ . The vectors  $\mathbf{u}_i$  and  $\mathbf{v}_i$  are defined in terms of the rotation matrix  $\mathcal{R}$  by using the Rodrigues formula [43]

$$\begin{aligned} u_i^\beta &= \mathcal{R}_i^{\beta 1} + i\mathcal{R}_i^{\beta 2}, \\ v_i^\beta &= \mathcal{R}_i^{\beta 3}, \end{aligned} \quad (7)$$

where  $\beta$  runs over  $\{x, y, z\}$ . The exchange tensor  $\mathcal{J}_{ij}$  reads

$$\begin{aligned} \mathcal{J}_{ij} &= J_{ij} \mathcal{I} + \mathcal{J}_{ij}^S + \mathcal{J}_{ij}^A \\ &= \begin{pmatrix} J_{ij} + \Gamma_{ij}^{xx} & D_{ij}^z & -D_{ij}^y \\ -D_{ij}^z & J_{ij} + \Gamma_{ij}^{yy} & D_{ij}^x \\ D_{ij}^y & -D_{ij}^x & J_{ij} - \Gamma_{ij}^{xx} - \Gamma_{ij}^{yy} \end{pmatrix}. \end{aligned} \quad (8)$$

After Fourier transform, the Hamiltonian in Eq. (6) can be recast in the following form:

$$\begin{aligned} \mathcal{H} = & \sum_{\mathbf{k} \in \text{BZ}} \left( a_i^\dagger(\mathbf{k}) a_i(-\mathbf{k}) \right) \begin{pmatrix} A(\mathbf{k}) - C & B(\mathbf{k}) \\ B^\dagger(\mathbf{k}) & \bar{A}(-\mathbf{k}) - C \end{pmatrix} \begin{pmatrix} a_i(\mathbf{k}) \\ a_i^\dagger(-\mathbf{k}) \end{pmatrix}, \end{aligned}$$

TABLE III. Matrix elements of the *ab initio* model Hamiltonian (meV) for  $\text{Sm}_2\text{Ir}_2\text{O}_7$ , as obtained by spin-orbit MRCI. The two-site singlet and (split) triplet states are labeled  $|\tilde{s}\rangle$  and  $\{|t_x\rangle, |t_y\rangle, |\tilde{t}_z\rangle\}$ , respectively.  $|\tilde{s}\rangle$  and  $|\tilde{t}_z\rangle$  are admixtures of ‘pure’  $|0, 0\rangle$  and  $|1, 0\rangle$  spin functions.

$H_{ab}^{kl}$ <i>initio</i>	$ \tilde{s}\rangle$	$ \tilde{t}_z\rangle$	$ t_y\rangle$	$ t_x\rangle$
$\langle\tilde{s} $	0	0	$-0.507i \mu_B h_{x'}$	$-0.296i \mu_B h_{y'}$
$\langle\tilde{t}_z $	0	21.414	$-1.294i \mu_B h_{x'}$	$-2.231i \mu_B h_{y'}$
$\langle t_y $	$0.507i \mu_B h_{x'}$	$1.294i \mu_B h_{x'}$	22.773	$1.896i \mu_B h_{z'}$
$\langle t_x $	$0.296i \mu_B h_{y'}$	$2.231i \mu_B h_{y'}$	$-1.896i \mu_B h_{z'}$	23.512

TABLE IV. Matrix form of the effective spin Hamiltonian in the basis of zero-field eigenstates.  $\Gamma_{2z'\pm x'}$  stands for  $2\Gamma_{z'z'} \pm \Gamma_{x'x'}$ ; expressions for the  $\Delta_+$  and  $\Delta_-$  terms are provided in Eq. (4).

$H_{\text{eff}}^{kl}$	$ \tilde{s}\rangle$	$ t_z\rangle$	$ t_y\rangle$	$ t_x\rangle$
$\langle\tilde{s} $	0	0	$-\frac{ih_{x'}(2Dg_{x'x'}+g_{x'y'}\Delta_+)}{\sqrt{4D^2+\Delta_+^2}}$	$-\frac{ih_{y'}(2Dg_{y'y'}-g_{x'y'}\Delta_+)}{\sqrt{4D^2+\Delta_+^2}}$
$\langle\tilde{t}_z $	0	$\frac{1}{2}\sqrt{4D^2+(2J+\Gamma_{x'x'})^2}$	$-\frac{ih_{x'}(2Dg_{x'x'}+g_{x'y'}\Delta_-)}{\sqrt{4D^2+\Delta_-^2}}$	$-\frac{ih_{y'}(2Dg_{y'y'}-g_{x'y'}\Delta_-)}{\sqrt{4D^2+\Delta_-^2}}$
$\langle t_y $	$\frac{ih_{x'}(2Dg_{x'x'}+g_{x'y'}\Delta_+)}{\sqrt{4D^2+\Delta_+^2}}$	$\frac{ih_{x'}(2Dg_{x'x'}+g_{x'y'}\Delta_-)}{\sqrt{4D^2+\Delta_-^2}}$	$\frac{1}{4}(2J+\Gamma_{2z'+x'}+\sqrt{4D^2+(2J+\Gamma_{x'x'})^2})$	$ig_{z'z'}h'_{z'}$
$\langle t_x $	$\frac{ih_{y'}(2Dg_{y'y'}+g_{x'y'}\Delta_+)}{\sqrt{4D^2+\Delta_+^2}}$	$\frac{ih_{y'}(2Dg_{y'y'}-g_{x'y'}\Delta_-)}{\sqrt{4D^2+\Delta_-^2}}$	$-ig_{z'z'}h_{z'}$	$\frac{1}{4}(2J+\Gamma_{2z'-x'}+\sqrt{4D^2+(2J+\Gamma_{x'x'})^2})$

where  $A$ ,  $B$ , and  $C$  are defined as :

$$A(\mathbf{k})_{ij} = \frac{\sqrt{s_i s_j}}{2} \mathbf{u}_i^T \mathcal{J}_{ij}(-\mathbf{k}) \bar{\mathbf{u}}_j, \quad (9)$$

$$B(\mathbf{k})_{ij} = \frac{\sqrt{s_i s_j}}{2} \mathbf{u}_i^T \mathcal{J}_{ij}(-\mathbf{k}) \mathbf{u}_j, \quad (10)$$

$$C(\mathbf{k})_{ij} = \delta_{ij} \sum_l s_l \mathbf{v}_i^T \mathcal{J}_{il}(0) \mathbf{v}_l. \quad (11)$$

This is diagonalized by using a Bogoliubov transformation [44]. The calculated eigenvalues are the eigenfrequencies of the spin waves and are plotted in Figs. 3, 4.(a)-(b), and S1.

[1] A. Kitaev, “Anyons in an exactly solved model and beyond,” *Ann. Phys.* **321**, 2 – 111 (2006).  
[2] G. Jackeli and G. Khaliullin, “Mott Insulators in the Strong Spin-Orbit Coupling Limit: From Heisenberg to a Quantum Compass and Kitaev Models,” *Phys. Rev. Lett.* **102**, 017205 (2009).  
[3] Y. Yamaji, Y. Nomura, M. Kurita, R. Arita, and M. Imada, “First-Principles Study of the Honeycomb-Lattice Iridates  $\text{Na}_2\text{IrO}_3$  in the Presence of Strong Spin-Orbit Interaction and Electron Correlations,” *Phys. Rev. Lett.* **113**, 107201 (2014).  
[4] V. M. Katukuri, S. Nishimoto, V. Yushankhai, A. Stoyanova, H. Kandpal, S. Choi, R. Coldea, I. Rousochatzakis, L. Hozoi, and J. van den Brink, “Kitaev interactions between  $j = 1/2$  moments in honeycomb  $\text{Na}_2\text{IrO}_3$  are large and ferromagnetic: insights from *ab initio* quan-

tum chemistry calculations,” *New J. Phys.* **16**, 013056 (2014).  
[5] B. H. Kim, G. Khaliullin, and B. I. Min, “Magnetic Couplings and Optical Spectra and Spin-Orbit Exciton in 5d Electron Mott Insulator  $\text{Sr}_2\text{IrO}_4$ ,” *Phys. Rev. Lett.* **109**, 167205 (2012).  
[6] N. B. Perkins, Y. Sizyuk, and P. Wölfle, “Interplay of many-body and single-particle interactions in iridates and rhodates,” *Phys. Rev. B* **89**, 035143 (2014).  
[7] N. A. Bogdanov, V. M. Katukuri, J. Romhányi, V. Yushankhai, V. Kataev, B. Büchner, J. van den Brink, and L. Hozoi, “Orbital reconstruction in nonpolar tetravalent transition-metal oxide layers,” *Nat. Commun.* **6**, 7306 (2015).  
[8] D. Coffey, T. M. Rice, and F. C. Zhang, “Dzyaloshinskii-Moriya interaction in the cuprates,” *Phys. Rev. B* **44**, 10112 (1991).  
[9] L. Shekhtman, O. Entin Wohlman, and A. Aharony, “Moriya’s anisotropic superexchange interaction, frustration, and Dzyaloshinsky’s weak ferromagnetism,” *Phys. Rev. Lett.* **69**, 836 (1992).  
[10] T. Yildirim, A. B. Harris, A. Aharony, and O. Entin-Wohlman, “Anisotropic spin Hamiltonians due to spin-orbit and Coulomb exchange interactions,” *Phys. Rev. B* **52**, 10239 (1995).  
[11] S. Disseler, *Phd Thesis*, Boston College (2013).  
[12] V. M. Katukuri, V. Yushankhai, L. Siurakshina, J. van den Brink, L. Hozoi, and I. Rousochatzakis, “Mechanism of Basal-Plane Antiferromagnetism in the Spin-Orbit Driven Iridate  $\text{Ba}_2\text{IrO}_4$ ,” *Phys. Rev. X* **4**, 021051 (2014).  
[13] M. Pererio, D. Yudin, J. Chico, C. Etz, O. Eriksson, and A. Bergman, “Topological excitations in a kagome magnet,” *Nat. Commun.* **5**, 4815 (2014).  
[14] B. J. Yang and N. Nagaosa, “Emergent Topological Phe-

- nomena in Thin Films of Pyrochlore Iridates,” *Phys. Rev. Lett.* **112**, 246402 (2014).
- [15] X. Hu, Z. Zhong, and G. A. Fiete, “First Principles Prediction of Topological Phases in Thin Films of Pyrochlore Iridates,” *Sci. Rep.* **5**, 11072 (2015).
- [16] Y. Yamaji and M. Imada, “Metallic interface emerging at magnetic domain wall of antiferromagnetic insulator: Fate of extinct weyl electrons,” *Phys. Rev. X* **4**, 021035 (2014).
- [17] P. Laurell and G. A. Fiete, “Topological magnon bands and unconventional superconductivity in pyrochlore iridate thin films,” [arXiv:1609.03612](https://arxiv.org/abs/1609.03612) (2016).
- [18] K. Tomiyasu, K. Matsuhira, K. Iwasa, M. Watahiki, S. Takagi, M. Wakeshima, Y. Hinatsu, M. Yokoyama, K. Ohoyama, and K. Yamada, “Emergence of Magnetic Long-range Order in Frustrated Pyrochlore  $\text{Nd}_2\text{Ir}_2\text{O}_7$  with Metal-Insulator Transition,” *J. Phys. Soc. Jpn.* **81**, 034709 (2012).
- [19] K. Ueda, J. Fujioka, B. J. Yang, J. Shiogai, A. Tsukazaki, S. Nakamura, S. Awaji, N. Nagaosa, and Y. Tokura, “Magnetic Field-Induced Insulator-Semimetal Transition in a Pyrochlore  $\text{Nd}_2\text{Ir}_2\text{O}_7$ ,” *Phys. Rev. Lett.* **115**, 056402 (2015).
- [20] Z. Tian, Y. Kohama, T. Tomita, H. Ishizuka, T. H. Hsieh, J. J. Ishikawa, K. Kindo, L. Balents, and S. Nakatsuji, “Field-induced quantum metal-insulator transition in the pyrochlore iridate  $\text{Nd}_2\text{Ir}_2\text{O}_7$ ,” *Nat. Phys.* **12**, 134 (2015).
- [21] E. Lefrancois, V. Simonet, R. Ballou, E. Lhote, A. Hadj-Azzem, S. Kodjikian, P. Lejay, P. Manuel, D. Khalyavin, and L. ?C. Chapon, “Anisotropy-Tuned Magnetic Order in Pyrochlore Iridates,” *Phys. Rev. Lett.* **114**, 247202 (2015).
- [22] H. Sagayama, D. Uematsu, T. Arima, K. Sugimoto, J. J. Ishikawa, E. O’Farrell, and S. Nakatsuji, “Determination of long-range all-in-all-out ordering of  $\text{Ir}^{4+}$  moments in a pyrochlore iridate  $\text{Eu}_2\text{Ir}_2\text{O}_7$  by resonant x-ray diffraction,” *Phys. Rev. B* **87**, 100403 (2013).
- [23] C. Donnerer, M. C. Rahn, M. Moretti-Sala, J. G. Vale, D. Pincini, J. Strempler, M. Krisch, D. Prabhakaran, A. T. Boothroyd, and D. F. McMorrow, “All-in-all-Out Magnetic Order and Propagating Spin Waves in  $\text{Sm}_2\text{Ir}_2\text{O}_7$ ,” *Phys. Rev. Lett.* **117**, 037201 (2016).
- [24] N. Taira, M. Wakeshima, and Y. Hinatsu, “Magnetic properties of iridium pyrochlores  $\text{R}_2\text{Ir}_2\text{O}_7$  ( $\text{R} = \text{Y}, \text{Sm}, \text{Eu}$  and  $\text{Lu}$ ),” *J. Phys.: Condens. Matter* **13**, 5527 (2001).
- [25] T. Helgaker, P. Jorgensen, and J. Olsen, *Molecular Electronic-Structure Theory* (Wiley, Chichester, 2000).
- [26] L. Hozoi, H. Gretarsson, J. P. Clancy, B.-G. Jeon, B. Lee, K. H. Kim, V. Yushankhai, P. Fulde, D. Casa, T. Gog, J. Kim, A. H. Said, M. H. Upton, Y. J. Kim, and J. van den Brink, “Longer-range lattice anisotropy strongly competing with spin-orbit interactions in pyrochlore iridates,” *Phys. Rev. B* **89**, 115111 (2014).
- [27] R. Yadav, N. A. Bogdanov, V. M. Katukuri, S. Nishimoto, J. van den Brink, and L. Hozoi, “Kitaev exchange and field-induced quantum spin-liquid states in honeycomb  $\alpha\text{-RuCl}_3$ ,” *Sci. Rep.* **6**, 37925 (2016).
- [28] K. Matsuhira, M. Wakeshima, Y. Hinatsu, and S. Takagi, “Metal-Insulator Transitions in Pyrochlores Oxides  $\text{Ln}_2\text{Ir}_2\text{O}_7$ ,” *J. Phys. Soc. Jpn.* **80**, 094701 (2011).
- [29] S. Kirkpatrick, C. D. Gelatt, and Jr. M. P. Vecchi, “Optimization by simulated annealing,” *Science* **220**, 671 (1983).
- [30] B. Skubic, J. Hellsvik, L. Nordström, and O. Eriksson, “A method for atomistic spin dynamics simulations: implementation and examples,” *J. Phys.: Condens. Matter* **20**, 315203 (2008).
- [31] N. A. Bogdanov, V. M. Katukuri, H. Stoll, J. van den Brink, and L. Hozoi, “Post-perovskite  $\text{CaIrO}_3$ : A  $j = 1/2$  quasi-one-dimensional antiferromagnet,” *Phys. Rev. B* **85**, 235147 (2012).
- [32] S. Nishimoto, V. M. Katukuri, V. Yushankhai, H. Stoll, U. K. Röbber, L. Hozoi, I. Rousochatzakis, and J. van den Brink, “Strongly frustrated triangular spin lattice emerging from triplet dimer formation in honeycomb  $\text{Li}_2\text{IrO}_3$ ,” *Nat. Commun.* **7**, 10273 (2016).
- [33] D. Figgien, K. A. Peterson, M. Dolg, and H. Stoll, “Energy-consistent relativistic pseudopotentials and correlation consistent basis sets for the 5d elements Hf–Pt,” *J. Chem. Phys.* **130**, 164108 (2009).
- [34] T. H. Dunning, “Gaussian basis sets for use in correlated molecular calculations. I. The atoms boron through neon and hydrogen,” *J. Chem. Phys.* **90**, 1007 (1989).
- [35] A. Berning, M. Schweizer, H.-J. Werner, P. J. Knowles, and P. Palmieri, “Spin-orbit matrix elements for internally contracted multireference configuration interaction wavefunctions,” *Mol. Phys.* **98**, 1823 (2000).
- [36] H.-J. Werner and P. J. Knowles, “An efficient internally contracted multiconfiguration-reference configuration interaction method,” *J. Chem. Phys.* **89**, 9 (1988).
- [37] P. J. Knowles and H.-J. Werner, “Internally contracted multiconfiguration-reference configuration interaction calculations for excited states,” *Theor. Chim. Acta* **84**, 95 (1992).
- [38] J. Pipek and P. G. Mezey, “A fast intrinsic localization procedure applicable for abinitio and semiempirical linear combination of atomic orbital wave functions,” *J. Chem. Phys.* **90**, 9 (1989).
- [39] H. J. Werner, P. J. Knowles, G. Knizia, F. R. Manby, and M. Schütz, “Molpro: a general-purpose quantum chemistry program package,” *Wiley Rev: Comp. Mol. Sci.* **2**, 242 (2012).
- [40] N. J. Hill, “Electron paramagnetic resonance of osmium-doped trichlorotris(diethylphenylphosphine) rhodium (III),” *J. Chem. Soc., Faraday Trans. 2* **68**, 427 (1972).
- [41] M. Oshikawa and I. Affleck, “Field-induced gap in  $S = 1/2$  antiferromagnetic chains,” *Phys. Rev. Lett.* **79**, 2883 (1997).
- [42] S. Toth and B. Lake, “Linear spin wave theory for single-Q incommensurate magnetic structures,” *J. Phys.: Condens. Matter* **27**, 166002 (2015).
- [43] O. Rodrigues, “Des lois géométriques qui régissent les déplacements d’un système solide dans l’espace, et de la variation des coordonnées provenant de ces déplacements considérés indépendamment des causes qui peuvent les produire,” *Journal de Mathématiques* **5**, 380-440 (1840).
- [44] J. Colpa, “Diagonalization of the quadratic boson Hamiltonian,” *Physica A* **93**, 327 (1978).